Title
Photo-induced force microscopy and sepctroscopy

Permalink
https://escholarship.org/uc/item/84g776h2

Author
Jahng, Junghoon

Publication Date
2015

Peer reviewed|Thesis/dissertation

UNIVERSITY OF CALIFORNIA,
IRVINE

Photo-induced force microscopy and spectroscopy

THESIS

submitted in partial satisfaction of the requirements
for the degree of

MASTER OF SCIENCE

in Physics

by

Junghoon Jahng

Thesis Committee:
Associate Professor Eric Olaf Potma, Chair
Professor H. Kumar Wickramasinghe
Professor Vartkess A. Apkarian

2015

DEDICATION

To

my parents and friends

in recognition of their worth

an apology

"You Only Live Once"

TABLE OF CONTENTS

LIST OF FIGURES

ACKNOWLEDGMENTS

ABSTRACT OF THE DISSERTATION

Photo-induced force microscopy and spectroscopy

By

Junghoon Jahng

Master of Science in Physics

University of California, Irvine, 2015

Associate Professor Eric Olaf Potma, Chair

Chapter 1

Introduction

The light-matter interaction has been at the heart of major advances from the atomic scale to the microscopic scale over the past four decades [1]. The demonstration of mechanically acting upon small particles with radiation pressure was done by Ashkin [2]. The light-induced force can trap and manipulate the micro-object, cool down the temperature of molecules such as the Bose-Einstein condensation. In particular, the ability to move colloidal microparticles has led to some spectacular and farreaching advances in the biological sciences. However, the spatial resolution is limited to the diffraction limit $\lambda/(2NA)$, where λ is the wavelength and NA is numerical aperture. Because of that, most of the experimental works are microscale or many bodies.

Atomic force microscopy (AFM) generates images based on variations in the local forces between an atomic tip and the surface specimen. The nanoscopic resolution provided by AFM yields topographic images with exquisite detail, enabling visualization of individual atoms and intermolecular bonds under optimized conditions [3, 4]. Yet, it hasn't been measured the contrast based on optically and chemically selective information, rendering the AFM contrast largely insensitive to the chemical and optical details of the sample.

In this regard, recent developments in combining light-induced molecular excitations with mechanical force detection are of particular interest, as these approaches seek to add chemical selectivity to force microscopy. A successful example in this category of techniques is infrared (IR) absorption AFM, also referred to as the photo-thermal induced resonance technique [5, 6, 7, 8, 9]. In this technique, the sample is illuminated with infrared light, producing heating of the material through direct excitation of dipole allowed vibrational transitions. The thermal expansion that follows is selective to spectroscopic transitions and can be probed with high spatial resolution through contact-mode AFM [6]. IR-based AFM has been used successfully to visualize molecular layers on surfaces with chemical selectivity and with a spatial resolution down to 25 nm [9].

An alternative method is photo-induced force microscopy, which probes the photo-induced changes in the dipolar interactions between a sharp polarizable tip and the sample [10, 11]. Unlike IR-AFM, the contrast in photo-induced force microscopy does not rely on the thermal expansion of the material. Rather, the technique is directly sensitive to the electromagnetic forces at play in the tip-sample junction, and can, in principle, be conducted in non-contact mode AFM. The advantage of this approach is that optical transitions can be probed directly as dissipation of excitation energy in the material is not required for generating contrast. In addition, the photo-induced forces are spatially confined and fundamentally decoupled from heat diffusion, giving rise to a high spatial resolution of 10 nm or better [11]. Theoretically, the spectroscopic information probed in this technique is akin to information accessible through coherent optical spectroscopy with heterodyne detection [12]. Photo-induced force microscopy has been successfully demonstrated through linear excitation of dipole-allowed electronic transitions [10] as well as nonlinear excitation of Raman-active transitions [11].

Although photo-induced force microscopy is a promising technique, the current theoretical understanding of the relevant forces in the tip-sample junction is rudimentary at best. In this contribution, we provide a simple description of the operating principle of the photo-induced

force microscope in terms of classical fields and forces. By including both the attractive gradient interactions and the repulsive scattering force, we simulate the characteristics of the force-distance curve and compare the predicted profile with experimental results obtained from gold nanowires and molecular nanoclusters. Our study identifies the distance regimes in which attractive gradient forces are dominant and points out under which conditions molecular selective signals are optimized. Finally, our experiments show that the technique can be carried out in femtosecond illumination mode, paving the way for more advanced nonlinear optical investigations at the nanoscale level.

Chapter 2

Theory of photo-induced force microscopy

2.1 Time-averaged Lorentz force: gradient and scattering force

We consider a monochromatic electromagnetic wave with angular frequency ω, which is incident on a polarizable particle in Fig. 2.1 (a). The time harmonic electric and magnetic field components at location $\mathbf{r}$ can be written as:

$$\mathbf{E}(\mathbf{r}, t) = \Re \left\{ \mathbf{E}(\mathbf{r})e^{-i\omega t} \right\} \tag{2.1}$$

$$\mathbf{B}(\mathbf{r}, t) = \Re \left\{ \mathbf{B}(\mathbf{r})e^{-i\omega t} \right\} \tag{2.2}$$

To the first order in the fields, the induced dipole moment of the particle assumes the same time dependence and is given as:

$$\vec{\mu}(\mathbf{r}, t) = \Re\left\{\vec{\mu}(\mathbf{r})e^{-i\omega t}\right\}$$

We assume that the particle has no static dipole moment. In this case, to the first order, the induced dipole moment is proportional to the electric field at the particle's position $\mathbf{r}$

$$\vec{\mu}(\mathbf{r}) = \alpha(\omega)\mathbf{E}(\mathbf{r}) \tag{2.3}$$

where α denotes the polarizability of a particle. For polarizable point dipoles located on a cubic lattice, the Clausius-Mossotti relation is exact in the zero-frequency limit, but is no exact at finite frequencies. The motion of charged particles in external force fields necessarily involves the emission of radiation whenever the charges are accelerated. Since we will be considering only periodic electric fields, it is straightforward to allow for the "radiative reaction" by assuming that, in addition to the electric fields due to other sources, each dipole is exposed to a "radiative reaction" electric field $\mathbf{E}_{rad} = \frac{2}{3}ik^3\mathbf{P}$ (Jackson,"Classical Electrodynamics", Ch.16, 1975), in which case

$$\mathbf{P} = \alpha\mathbf{E} = \alpha_0(\mathbf{E}_{int} + \mathbf{E}_{rad}) \tag{2.4}$$

where α_0 satisfies the Clausius-Mossotti equation as

$$\alpha_0 = 4\pi\varepsilon_0\varepsilon_m\left(\frac{\varepsilon_p - \varepsilon_m}{\varepsilon_p + 2\varepsilon_m}\right)a^3 \tag{2.5}$$

where a is the particle radius and ε_p is the relative permittivity of the particle and ε_m is the relative permittivity of the medium. which implies a polarizability (now assuming that the

coordinate system is chosen so that α_0 is diagonalized)

$$\alpha = \frac{\alpha_0}{1 - ik^3\alpha_0/(6\pi\varepsilon_0\varepsilon_m)} \equiv \alpha' + i\alpha'' \tag{2.6}$$

where where α' is a real part of a particle polarizability and α'' is a imaginary part of a particle polarizability. The polarizability differs from Eq. (2.5) only through the term inversely proportional to $ik^3\alpha_0/(6\pi\varepsilon_0\varepsilon_m)$, which clearly vanishes in the zero frequency limit $(k \to 0)$ or the continuum limit $a \to \infty$. This "radiative reaction" corection will generally be a minor one in those cases where the discrete dipole model provides a good approximation. Generally, α is a tensor of rank two, but for atoms and molecules it is legitimate to use a scalar representation since only the projection of $\vec{\mu}$ along the direction of the electric field is of direct relevance. Using the discrete dipole approximation for calculating the force on the tip, the cycle-averaged Lorentz force is [13]

$$\langle \mathbf{F}_{pif}(z) \rangle = \frac{\alpha'}{2} \nabla \left\langle |\mathbf{E}|^2 \right\rangle + \omega \alpha'' \left\langle \mathbf{E} \times \mathbf{B} \right\rangle \tag{2.7}$$

The first term of Eq. (2.7) is recognized as the gradient force (or optical tweezer force) and the second term is denoted the scattering or absorption force. The gradient force originates from field inhomogeneities, and is proportional to the dispersive part (real part) of the complex polarizability. On the other hand, the scattering or absorption force is proportional to the dissipative part (imaginary part) of the complex polarizability. Eq. 2.7 is a general description of the force for the spatial variation of the field between the particle and the tip dipoles.[13]

2.1.1   Gradient force

The gradient forces in the tip-sample junction are considered as three kinds of cases. The first case is that the tip is illuminated by the beam in free space in Fig. 2.1(a). In this case,
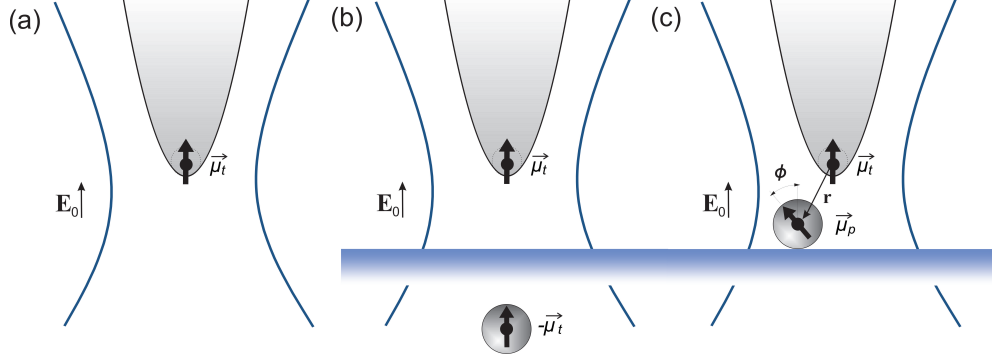
Figure 2.1: Graphical representation of the symbols used to derive the photo-induced force in the dipolar limit. (a) optical tweezer force (b) image dipole force (c) photo-induced force (optical binding). **r** denotes the center of mass coordinate.

the force is due to the field gradient of the incident light. The light field directly interact to tip. If the plane wave is illuminated to the tip with the point dipole approximation, the gradient force is gone. However, if a gaussian beam is applied, the tip is suffered an attractive force toward the focus of light such as optical tweezer force. Fig. 2.1(b) shows the second case which that the tip is approached to an infinite metal plane. In this case there is a multiple reflection between the tip and sample. The multiple reflected field can be considered as originating from an image dipole in the metal plane. Therefore the gradient force is the field gradient force between the induced dipole and the image dipole. When we look up the z-directional image dipole force, it is made up of by two parts with respect to z- and x-directional electric field. Because the azimuthal symmetry y-directional field is same to the x-directional field. Both of the z-directional image dipole forces are always negative (attractive) force because the sign of the image dipoles are the flipped one of the induced dipoles. The mathematical details are well described in Sec. 2.2. The last case is that the tip is approached to a molecule on a dielectric place surface such as figure 2.1(c). The incident beam induces dipoles on both of the tip and the molecule, and then the dipole-dipole interaction is happened. This dipole-dipole interaction is a mutual interaction which means each of the induced dipole exerts electric field and then the fields induce again each of them. Some researchers called this force as optical binding force. The z-directional optical binding

force is also analyzed with respect to the z- and x-directional electric field. In the z-direction, each of the dipoles are aligned with respect to z-direction so that the z-directional dipole-dipole force is negative (attractive). On the other hand, the x-directional field induces each of the dipole in the same x-direction so that their dipole-dipole interaction force in z-direction is positive (repulsive). We will discuss more of the details in Sec. 2.3.

2.1.2   Scattering force

Besides the gradient force, Eq. (2.7) predicts another photo-induced force. This second contribution is recognized as the scattering force, which is generally repulsive. The magnitude of the scattering force is proportional to the dissipative part of the interaction of light with the polarizable particles, as described by the imaginary part of the complex polarizability. From the Eq. (2.7), the scattering force can be described as:

$$\langle \mathbf{F}_{sc} \rangle_z = \omega \alpha_t'' \langle \mathbf{E}_0 \times \mathbf{B}_0 \rangle_z \tag{2.8}$$

where $\mathbf{B}_0 = B_{0x}\hat{x} + B_{0y}\hat{y} + B_{0z}\hat{z}$. Only the transverse electric and magnetic field components contribute to the the force along the z-direction. Given that the dominant component of the incident field is polarized along x, i.e. $\mathbf{E_0} \approx E_{0x}\hat{x}$, the absorption force can be written as:

$$\langle \mathbf{F}_{sc} \rangle_z = \frac{2\pi \alpha_t''}{\lambda} E_{0x}^2 \tag{2.9}$$

where λ is the wavelength of the incident beam. Unlike the gradient force, the scattering force is repulsive. In addition, whereas the gradient force is expected to scale as z^{-4} with tip-sample distance, the distance-dependence of the scattering force is implicitly contained in the spatial extent of the excitation field E_{0x}. Because the axial dimension of the excitation field is in the (sub)-μm range, the scattering force manifests itself over a different spatial scale than the local gradient force. We expect, therefore, that the short range nanoscopic

interactions are governed by the gradient force, while at longer distances the scattering force is dominant. Note that the magnitude of the total optical force may exhibit a minimum at the tip-sample distance where the attractive gradient force and the repulsive scattering force cancel.

2.2 Image dipole force

In section 2.1, the force equation 2.7 is the direct force acting on the polarizable particle with light. The incident field inhomogeneity make a gradient force on the particle and the light momentum generate a scattering force on the particle. In this section we discuss about the tip-substrate case. Fig. 2.1 (b), there is a diagram about the tip-substrate case. In this case the multiple reflection between the tip and sample is considered which is generally described with Maxwell tensor but also simply assumed as the image dipole. If we assume the image dipole below the substrate, the multiple interaction can be modeled by considering both the tip and substrate as spherical particles of volume $\frac{4\pi}{3}a_t^3$ and an effective polarizability α_t. Fig. 2.2 (b) and Fig. 2.3 (b) show the z- and x- oriented tip dipole above a planar interface and its image dipoles in the medium. For the perfect metal, the distance from surface and the magnitude of the image dipole moments are the same as for the primary dipole. However, the sign of the image dipole is different. $\mathbf{E}_t$ and $\mathbf{E}'_t$ are the electric fields from the tip and the image dipole, respectively.

2.2.1 Vertical image dipole

For a dipole $\mu_t = \mu_{t_z}\hat{\mathbf{n}}_z$, the evaluation of the electric field in Cartesian coordinates leads to

$$\mathbf{E}_t = \frac{\mu_{t_z}}{4\pi\varepsilon_0\varepsilon_1}\left[\frac{3x(z-h)}{r^5}, \frac{3y(z-h)}{r^5}, \frac{3(z-h)^2}{r^5} - \frac{1}{r^3}\right] \tag{2.10}$$

9

Figure 2.2: Graphical representation of three kinds of the z-directional gradient forces in longitudinal electric field. (a) optical tweezer force (b) image dipole force (c) photo-induced force (optical binding). $\mathbf{r}$ denotes the center of mass coordinate.

where h is the height of the dipole above the interface. Assuming an image dipole $\mu_t = \mu_{t_z}\hat{\mathbf{n}}_z$, a similar expression can be derived for the image field $\mathbf{E}'_t$

$$\mathbf{E}'_t = \frac{\mu_{t_z}}{4\pi\varepsilon_0\varepsilon_1}\left[\frac{3x(z+h)}{r'^5}, \frac{3y(z+h)}{r'^5}, \frac{3(z+h)^2}{r'^5} - \frac{1}{r'^3}\right] \tag{2.11}$$

where r′ denotes the radial distance measured from the location of the image dipole. A reasonable ansatz for the total field $\mathbf{E}$ in either of the two half-spaces is

$$\begin{aligned}\mathbf{E} = \quad &\mathbf{E}_0 + \mathbf{E}_t + \left(\frac{\varepsilon_2 - \varepsilon_1}{\varepsilon_2 + \varepsilon_1}\right)\mathbf{E}'_t \quad z > 0 \\ &\mathbf{E}_0 + \left(\frac{\varepsilon_1}{\varepsilon_2}\frac{2\varepsilon_2}{\varepsilon_2 + \varepsilon_1}\right)\mathbf{E}_t \quad z < 0\end{aligned} \tag{2.12}$$

At the $z = h, r = 0, r' = 2h = d$, the total electric field and the dipole moment are:

$$\mathbf{E} = E_{0_z}\hat{\mathbf{n}}_z + \left(\frac{\varepsilon_2 - \varepsilon_1}{\varepsilon_2 + \varepsilon_1}\right)\frac{\mu_{t_z}}{4\pi\varepsilon_0\varepsilon_1}\frac{2}{d^3}\hat{\mathbf{n}}_z \tag{2.13}$$

$$\mu_{t_z} = \alpha_{t_z}\mathbf{E} \tag{2.14}$$

By solving the above simultaneous equations, then inserting them into the force equation (2.7) we can obtain the z-directional image dipole force and scattering force on the polarizable

10

particle.

$$\langle \mathbf{F}_{image} \rangle_z = \frac{12\pi^2 \varepsilon_0^2 \varepsilon_1^2 \bar{\varepsilon}_r |\alpha_{t_z}|^2 E_{0_z}^2 d^5}{(\alpha_{t_z} \bar{\varepsilon}_r - 2\pi \varepsilon_0 \varepsilon_1 d^3)^3} \quad (2.15)$$

where λ is the wavelength of the incident beam and $\bar{\varepsilon}_r = (\varepsilon_2 - \varepsilon_1)/(\varepsilon_2 + \varepsilon_1)$. In the limit of $a_t^3 \ll d^3$ which is the point dipole approximation, the image dipole force is recast with setting $d \equiv z$ as:

$$\langle \mathbf{F}_{image} \rangle_z \simeq -\frac{3\bar{\varepsilon}_r |\alpha_{t_z}|^2 E_{0_z}^2}{2\pi \varepsilon_0 \varepsilon_1 z^4} \quad (2.16)$$

Unlike the scattering force, the image dipole force is attractive (negative). In addition, whereas the image dipole force is expected to scale as z^{-4} with tip-sample distance, the distance-dependence of the scattering force is implicitly contained in the spatial extent of the excitation field E_{0x}. Because the axial dimension of the excitation field is in the (sub)-μm range, the scattering force manifests itself over a different spatial scale than the local gradient force. We expect, therefore, that the short range nanoscopic interactions are governed by the gradient force, while at longer distances the scattering force is dominant. Note that the magnitude of the total optical force may exhibit a minimum at the tip-sample distance where the attractive gradient force and the repulsive scattering force cancel.

2.2.2   Horizontal image dipole

The procedure for a dipole $\mu_t = \mu_x \mathbf{n}_x$ is similar. The primary and the image fields turn out to be

$$\mathbf{E}_t = \frac{\mu_x}{4\pi \varepsilon_0 \varepsilon_1} \left[\frac{3x^2}{r^5} - \frac{1}{r^3}, \frac{3xy}{r^5}, \frac{3x(z-h)}{r^5} \right] \quad (2.17)$$

$$\mathbf{E}_t' = \frac{\mu_x}{4\pi \varepsilon_0 \varepsilon_1} \left[\frac{3x^2}{r'^5} - \frac{1}{r'^3}, \frac{3xy}{r'^5}, \frac{3x(z+h)}{r'^5} \right] \quad (2.18)$$
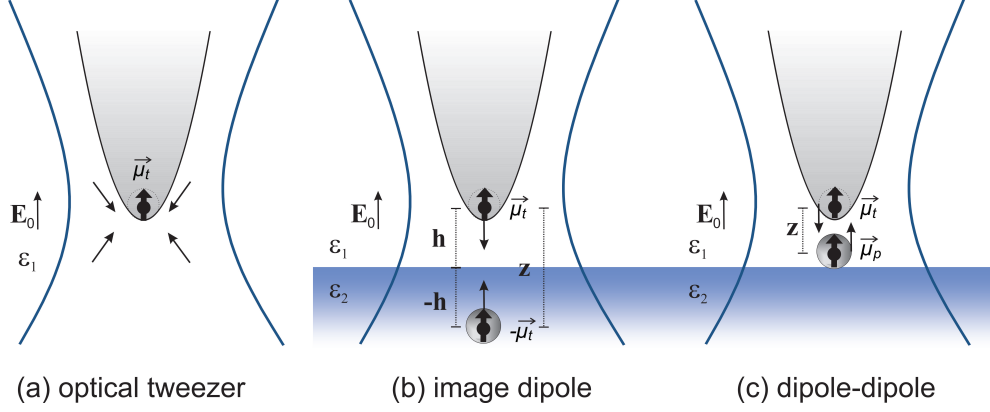
11
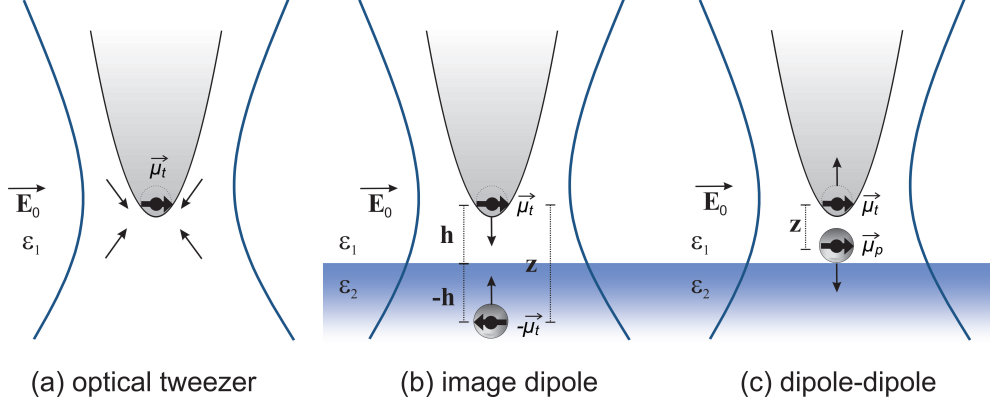
Figure 2.3: Graphical representation of three kinds of the z-directional gradient forces in longitudinal electric field. (a) optical tweezer force (b) image dipole force (c) photo-induced force (optical binding). $\mathbf{r}$ denotes the center of mass coordinate.

The corresponding ansatz for the total field $\mathbf{E}$ in either of the two half-spaces is

$$
\begin{aligned}
\mathbf{E} = \quad & \mathbf{E}_0 + \mathbf{E}_t - \left(\frac{\varepsilon_2 - \varepsilon_1}{\varepsilon_2 + \varepsilon_1}\right) \mathbf{E}_t' \quad z > 0 \\
& \mathbf{E}_0 + \left(\frac{\varepsilon_1}{\varepsilon_2} \frac{2\varepsilon_2}{\varepsilon_2 + \varepsilon_1}\right) \mathbf{E}_t \quad z < 0
\end{aligned}
\tag{2.19}
$$

Besides the sign of $\bar{\varepsilon}_r$, the parameters are identical with the parameters of the vertical dipole. At the $z = h, r = 0, r' = 2h = d$, the total x-directional electric field and the dipole moment are:

$$
\mathbf{E} = E_{0_x} + \left(\frac{\varepsilon_2 - \varepsilon_1}{\varepsilon_2 + \varepsilon_1}\right) \frac{\mu_{t_x}}{4\pi\varepsilon_0\varepsilon_1} \frac{1}{d^3} \hat{\mathbf{n}}_x
\tag{2.20}
$$

$$
\mu_{t_x} = \alpha_{t_x} \mathbf{E}
\tag{2.21}
$$

In the same manner with vertical image dipole case, the force equation (2.7) can be obtained as:

$$
\langle \mathbf{F}_{image} \rangle_z = \frac{48\pi^2 \varepsilon_0^2 \varepsilon_1^2 \bar{\varepsilon}_r |\alpha_{t_x}|^2 E_{0_x}^2 d^5}{(\alpha_{t_x}\bar{\varepsilon}_r - 4\pi\varepsilon_0\varepsilon_1 d^3)^3}
\tag{2.22}
$$

In the limit of $a_t^3 \ll d^3$ which is the point dipole approximation, the x-directional image dipole force is recast with setting $d \equiv z$ as:

$$\langle \mathbf{F}_{image} \rangle_z \simeq -\frac{3\bar{\varepsilon}_r |\alpha_{t_x}|^2 E_{0_x}^2}{4\pi\varepsilon_0\varepsilon_1 z^4} \tag{2.23}$$

2.3 Photo-induced force: optical binding between nanoparticles

The photo-induced gradient force between tip and sample is a mutual interaction force. The electric field experienced by the sample particle (molecule) is a combination of the incident electric field and the evanescent field of the induced dipole in the tip, and vice versa. In this section we use the classical model of induced oscillating dipoles to express the forces acting upon them in the case of the figure 2.1 (c).

2.3.1 Vertical dipole

For our discussion here, the forces in the z dimension dominate the cantilever response. We therefore consider $\vec{\mu}_t = \mu_{t_z}\hat{z}$ and $\vec{\mu}_p = \mu_{p_z}\hat{z}$, the z components of the dipole moment of the tip and molecule. Then the static electric fields of the induced dipoles are

$$\mathbf{E}_i = \frac{1}{4\pi\varepsilon_0}\frac{(3\vec{\mu_{i_z}} \cdot \mathbf{r})\,\mathbf{r} - \vec{\mu_{i_z}}}{r^3} \tag{2.24}$$

where $r = \sqrt{x^2 + y^2 + z^2}$, and $i = t, p$ respectively. The static dipole field is also defined as $\mathbf{E}_i \equiv E_{i_x}\hat{x} + E_{i_y}\hat{y} + E_{i_z}\hat{z}$. Because of the azimuthal symmetry, E_{i_x} is same to E_{i_y}. The z-component of the molecule's dipole moment and its corresponding electric field $\mathbf{E}_p$ can be

found as:

$$\mu_{p_z} = \frac{2z^3\pi\alpha_{p_z}\varepsilon_0(\alpha_{t_z} + 2z^3\pi\varepsilon_0)E_{0z}}{4z^6\pi^2\varepsilon_0^2 - \alpha_{p_z}\alpha_{t_z}} \tag{2.25}$$

$$E_{p_z} = \frac{\alpha_{p_z}(\alpha_{t_z} + 2z^3\pi\varepsilon_0)E_{0z}}{4z^6\pi^2\varepsilon_0^2 - \alpha_{p_z}\alpha_{t_z}} \tag{2.26}$$

with $\mathbf{E}_0 = E_{0x}\hat{x} + E_{0y}\hat{y} + E_{0z}\hat{z}$. The expressions (2.26) and (2.27) can be simplified when it is assumed that the distance between the tip and molecule is larger than the physical size of the particles, i.e. $z > a_t$ and $z > a_p$, called as point-dipole approximation. Because the polarizabilities of the tip and molecule scale with the cube of the particle radius, as in (2.5), we may also write $z^6 >> a_p^3 a_t^3$. Under these reasonable assumptions, the z-component of the gradient force is reduced to:

$$\langle \mathbf{F}_g \rangle_z \simeq -\frac{3Re[\alpha_{p_z}\alpha_{t_z}^*]}{2\pi\varepsilon_0 z^4}E_{0z}^2 - \frac{3Re[\alpha_{p_z}\alpha_{t_z}^{*\,2}]}{2\pi^2\varepsilon_0^2 z^7}E_{0z}^2 - \frac{3Re[\alpha_{p_z}^2\alpha_{t_z}^*]}{4\pi^2\varepsilon_0^2 z^7}E_{0z}^2. \tag{2.27}$$

We see from (2.16) and (2.24) that the image dipole force exhibits a z^{-4} dependence. It is thus a force that is expected to be prominent in only a narrow nanoscopic range of the tip-molecule distance, and less relevant for larger separations of molecule and tip. The negative sign in this interaction indicates that the force is attractive. Note that the strength of the force depends on the polarizability α_p of the sample particle. The expression in (2.28) is similar to the formula previously used in [10]. We will use the parameter $\beta = 3\alpha_p'\alpha_t'E_{0z}^2/2\pi\varepsilon_0$ to characterize the magnitude of the gradient force in a given measurement. Note that for the highly confined fields relevant to the tip-sample geometry, this approximation is debatable. Nonetheless, we assume that the image dipole force, as described by the component gradient and scattering forces in Eq. 2.28, captures the essential physics of the problem at hand.

2.3.2 Horizontal dipole

For our discussion here, the forces in the x dimension dominate the cantilever response. We therefore consider $\vec{\mu}_= \mu_{t_x}\hat{x}$ and $\vec{\mu}_p = \mu_{p_x}\hat{x}$, the z components of the dipole moment of the tip and molecule. Then the static electric fields of the induced dipoles are

$$\mathbf{E}_i = \frac{1}{4\pi\varepsilon_0}\frac{(3\vec{\mu_{i_x}}\cdot\mathbf{r})\,\mathbf{r} - \vec{\mu_{i_x}}}{r^3} \tag{2.28}$$

where $\mathbf{E}_i = E_{ix}\hat{x} + E_{iy}\hat{y} + E_{iz}\hat{z}$, $r = \sqrt{x^2 + y^2 + z^2}$, and $i = t, p$ respectively. Because of the azimuthal symmetry, E_{iz} is similar to E_{iy}. The z-component of the molecule's dipole moment and its corresponding electric field $\mathbf{E}_p$ can be found as:

$$\mu_{p_x} = \frac{4z^3\pi\alpha_{p_x}\varepsilon_0(\alpha_{t_x} + 2z^3\pi\varepsilon_0)E_{0x}}{4z^6\pi^2\varepsilon_0^2 - \alpha_{p_x}\alpha_{t_x}} \tag{2.29}$$

$$E_{p_x} = \frac{\alpha_{p_x}(\alpha_{t_x} - 4z^3\pi\varepsilon_0)E_{0x}}{16z^6\pi^2\varepsilon_0^2 - \alpha_{p_x}\alpha_{t_x}} \tag{2.30}$$

with $\mathbf{E}_0 = E_{0x}\hat{x} + E_{0y}\hat{y} + E_{0z}\hat{z}$.

$$\langle\mathbf{F}_g\rangle_x \simeq \frac{3Re[\alpha_{p_x}\alpha_{t_x}^*]}{4\pi\varepsilon_0 z^4}E_{0x}^2 - \frac{3Re[\alpha_{p_x}\alpha_{t_x}^{*\,2}]}{8\pi^2\varepsilon_0^2 z^7}E_{0x}^2 - \frac{3Re[\alpha_{p_x}^2\alpha_{t_x}^*]}{16\pi^2\varepsilon_0^2 z^7}E_{0z}^2. \tag{2.31}$$

2.4 Cantilever dynamics

2.4.1 Continuous beam model

The Euler-Bernoulli equation describes the bending of a rectangular and homogeneous cantilever along its longitudinal axis. The Euler-Bernoulli equation for a continuous and uniform
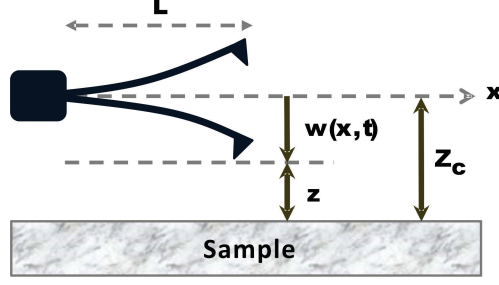
Figure 2.4: Graphical representation of the cantilever motion. z is the instantaneous position of cantilever. z_c is the average position, z_1 is the oscillation of fundamental resonance, and z_2 is the oscillation of the next resonance.

cantilever beam under the action of external forces applied at its free end is

$$EI\frac{\partial}{\partial x^4}\left[w(x,t) + a_1\frac{\partial w(x,t)}{\partial t}\right] + \rho bh\frac{\partial^2}{\partial t^2} = -a_0\frac{\partial w(x,t)}{\partial t} + \delta(x - L)[F_{ext}(t) + F_{ts}(d)] \quad (2.32)$$

where E is the cantilever's Young's modulus; I is the area moment of inertia; a_1 is the internal damping coefficient; ρ is the mass density; W , h and L are, respectively, the width, height, and length of the cantilever; a_0 is the hydrodynamic damping; $w(x,t)$ is the time-dependent vertical displacement of the differential beam's element placed at the x position (Fig. 2.4); F_{ext} is the excitation force; while the tip-surface interaction is represented by F_{ts} with

$$z = z_c + w(x,t) \quad (2.33)$$

as the instantaneous tip-surface separation. We substitute the ansatz $w(x,t) = \varphi(x)Y(t)$ in Eq. (2.33) and apply the following boundary conditions:

$\varphi(0) = 0$ (vertical displacement at x = 0 is zero),

$\varphi'(0) = 0$ (slope at x = 0 is zero),

$\varphi''(0) = 0$ (vertical internal torque at x = L is zero),

$\varphi'''(0) = 0$ (vertical internal force at x = L is zero).

The cantilever at x=0 is clamped [Eqs. (2.4.1) and (2.4.1)] while it is free at x=L [Eqs. (2.4.1) and (2.4.1)]. The above boundary conditions introduce a discrete number of solutions to Eq. (2.33), then the vertical displacement can be expanded into a series of eigenmodes,

$$w(x,t) = \sum_{n=1}^{\infty} \phi_n(x) Y_n(t) \tag{2.34}$$

Where can be defined as [26],

$$\phi_n(x) = \cos(\kappa_n \frac{x}{L}) - \cosh(\kappa_n \frac{x}{L}) - \frac{\cos(\kappa_n) + \cosh(\kappa_n)}{\sin(\kappa_n) + \sinh(\kappa_n)} [\sin(\kappa_n \frac{x}{L}) - \sinh(\kappa_n \frac{x}{L})] \tag{2.35}$$

with κ_n as the n-th positive real root of the equation

$$1 + \cos(\kappa_n) \cosh(\kappa_n) = 0 \tag{2.36}$$

$$\int_0^L \phi_n(x) \phi_m(x) dx = L \delta_{n,m} \tag{2.37}$$

$$\phi_n(0) = 0 \tag{2.38}$$

$$\phi_n(L) = 2(-1)^n. \tag{2.39}$$

On the other hand, the time-dependent function for each eigenmode, , obeys the set of anharmonic differential equations

$$m_n \ddot{Y}_n(t) + b_n \dot{Y}_n(t) + k_n Y_n(t) = F_n(t), \; n = 1, 2, 3 \ldots \tag{2.40}$$

where effective masses m_n, the effective damping coefficient given as $b_n = \frac{k_n}{\omega_n Q_n}$, eigenmode resonances ω_n, quality factors Q_n, the force constant k_n and external forces $F_n(t)$ of the n-th

eigenmode are defined by

$$\omega_n = \left(\frac{\alpha_n}{L}\right)^2 \frac{EI}{\rho W h} \tag{2.41}$$

$$m_n = \rho W h \int_0^L |\phi_n(x)|^2 dx = \rho W h L \equiv m_c, \tag{2.42}$$

$$Q_n = \frac{\omega_n}{\frac{a_0}{\rho W h} + a_1 \omega_n^2} \tag{2.43}$$

$$F_n(t) = \int_0^L f_{ext}(x,t)\phi_n(x)dx = \int_0^L \delta(x-L)[F_{ext}(t) + F_{ts}(z)]\phi_n(x)dx$$
$$= 2(-1)^n[F_{ext}(t) + F_{ts}(z)] \tag{2.44}$$

The total mass of the cantilever is expressed as m_c while $f_{ext}(x,t)$ represents the density of external forces per length. Then, the actual tip motion can be calculated as

$$w(L,t) = \sum_{n=1}^{\infty} \phi_n(L)Y_n(t) = \sum_{n=1}^{\infty} 2(-1)^n Y_n(t) \equiv \sum_{n=1}^{\infty} z_n(t) \tag{2.45}$$

where $z_n(t)$ is the modal projection of the tip motion. Combination of the above definitions and multiply $\phi_n(L)$ to Eq. (2.41) gives the corresponding differential equation for $z_n(t)$,

$$m\ddot{z}_n(t) + b_n\dot{z}_n(t) + k_n z_n(t) = F_{ext}(t) + F_{ts}(z), \ n = 1, 2, \dots \tag{2.46}$$

where $m = 0.25m_c$ It is shown then that the modal effective mass m is one fourth of the total mass of the cantilever. This is true whenever we deal with homogeneous and rectangular cantilevers. The above number coincides with the result given by Sader in Ref. [27]. Each mode is described by its modal parameters, eigenfrequency ω_n, spring constant $k_n = m\omega_n^2$, and quality factor Q_n.

2.4.2 Point-mass spring model

We next consider the dynamics of the cantilever-tip system in the presence of the photo-induced force $F_{pif} = F_g + F_{sc}$. The cantilever motion is modeled as a simple collection of independent point-mass harmonic oscillators, with motion confined to the z-coordinate only. In practice, two mechanical resonances are of relevance to the photo-induced force microscopy experiment, namely the first and a higher-order mechanical eigenmode of the cantilever-tip system. The first mechanical resonance is excited by the external driving force F_1 with frequency ω_1, whereas the higher-order resonance at ω_n is actively driven by F_{pif}. In addition, the cantilever-tip is subject to the interaction force F_{int}, which includes all relevant Van der waals, Casimir forces, electrostatic, magnetic force and so on [20, 16, 14]. In this model, the equations of motion for the displacement of the first (z_1) and higher-order (z_n) mode are found as:

$$m\ddot{z}_1 + b_1\dot{z}_1 + k_1 z_1 = F_1 \cos(\omega_1 t) + F_{pif}(z(t))(1 + \cos(\omega_n t)) + F_{int}(z(t)) \quad (2.47)$$

$$m\ddot{z}_n + b_n\dot{z}_n + k_n z_n = F_1 \cos(\omega_1 t) + F_{pif}(z(t))(1 + \cos(\omega_n t)) + F_{int}(z(t)) \quad (2.48)$$

where m is the effective mass of the cantilever; k_i and b_i are, respectively, force constant and the damping coefficient of the ith eigenmode [14]. In the following, we will set $n = 2$, corresponding to the tip displacement of the second mechanical resonance, but the analysis applies equally to higher-order modes. Note that the resonance frequency ω_i and the external driving force F_1 can be expressed as $\omega_i = \sqrt{k_i/m}$ and $F_1 = k_1 A_{01}/Q_1$, respectively, where A_{01} is the free oscillation amplitude of the driven first eigenmode of the cantilever, and Q_1 is the quality factor of the fundamental resonance. In addition, the damping coefficient can be expressed as $b_i = m\omega_i/Q_i$. The instantaneous tip-surface distance is represented by

$$
\begin{aligned}
z(t) \quad &= z_c + z_1(t) + z_2(t) + O(\varepsilon) \\
&\approx z_c + A_1 \sin(\omega_1 t + \theta_1) + A_2 \sin(\omega_2 t + \theta_2)
\end{aligned}
\quad (2.49)
$$

19

$$z(t) \approx z_c + A_1 \sin(\omega_1 t + \theta_1) + A_2 \sin(\omega_2 t + \theta_2) \tag{2.50}$$

where z_c is the equilibrium position of the cantilever, A_i is the amplitude and θ_i is the phase shift of the ith eigenmode; $O(\varepsilon)$ is a term that carries the contribution of the other modes and harmonics. Substituting Eq. (2.49) into Eqs. (2.48) and (2.49) by multiplying both sides of the resulting equation by $\sin(\omega_i t + \theta_i)$ and $\cos(\omega_i t + \theta_i)$, followed by an integration over the oscillation period, the following general relations for amplitude, phase, mechanical interaction force and photo-induced force are obtained:

$$(k_1 - m\omega_1{}^2)\frac{A_1}{2} = \frac{F_1}{2}\sin\theta_1 + \int_0^T F_{int}\sin(\omega_1 t + \theta_1)dt \tag{2.51}$$

$$\frac{b_1\omega_1 A_1}{2} = \frac{F_1}{2}\cos\theta_1 + \int_0^T F_{int}\cos(\omega_1 t + \theta_1)dt \tag{2.52}$$

$$(k_2 - m\omega_2{}^2)\frac{A_2}{2} = \int_0^T [F_{int} + F_{pif}\cos(\omega_2 t)]\sin(\omega_2 t + \theta_2)dt$$

$$\tag{2.53}$$

$$\frac{b_2\omega_2 A_2}{2} = \int_0^T [F_{int} + F_{pif}\cos(\omega_2 t)]\cos(\omega_2 t + \theta_2)dt \tag{2.54}$$

If the form of F_{int} and F_{pif} is known, the amplitudes A_1, A_2 and the phase shifts θ_1, θ_2 can be calculated through numerical integration of Eqs (2.51)-(2.54).

2.5 Reconstruction of distance-dependent force

The amplitude and phase of the first and second resonances are experimentally accessible quantities. We next describe an approximate method to relate the forces active at the tip-sample junction to these experimental quantities. In general, F_{int} is a nonlinear function of the tip-sample distance z and contains both conservative and dissipative (i.e., nonconservative) forces,

$$F_{int} = F_c(z) + F_{nc}, \tag{2.55}$$

where the conservative term F_c, by definition, depends only on the distance z which includes all relevant force potential such as Van der waals, Casimir forces, electrostatic, magnetic force and so on [20, 16, 14]]. For our description here, we assume that the nonconservative force can be written as $F_{nc} = -\Gamma(z)\dot{z}$, where Γ represents the effective damping coefficient of a given dissipative interaction. Such a form of force may describe many physical interactions such as the hydrodynamic or capillary meniscus forces[15, 16]. Note that although the term $-\Gamma(z)\dot{z}$ may be replaced by some other specific forms of dissipation, one can still employ the effective and intuitive coefficient Γ as a parameter describing a given dissipation [17, 18].

We use two approximations to simplify the description. First, we assume that the tip displacement is small such that the force at z can be obtained through a Taylor expansion of the force at the equilibrium position z_c. Under these conditions, the mechanical interaction force and the photo-induced force can be expressed by

$$
\begin{aligned}
F_{int}(z(t)) &= F_c(z) - \Gamma(z)\dot{z} \\
&\approx F_c(z_c) + \frac{\partial F_c(z)}{\partial z}|_{z_c}(z - z_c) - \Gamma(z_c)\dot{z} \quad\quad (2.56)
\end{aligned}
$$

$$
F_{pif}(z(t)) \approx F_{opt}(z_c) + \frac{\partial F_{pif}}{\partial z}|_{z_c}(z - z_c) \quad\quad (2.57)
$$

Second, we assume that the frequency of the first and second mechanical resonance are related as $\omega_2 \approx 6\omega_1$. In practice, the frequency of the 2nd resonance is $6.27\omega_1$ [14]. Although the approximation $\omega_2 \approx 6\omega_1$ gives rise to numerical differences in the integration of Eqs. (2.51)-(2.54), this difference is small while the general physics of the problem remains preserved. Using the approximation $\omega_2 \approx 6\omega_1$, the forces are simplified to

$$
F_c(z) = \int_z^\infty [\frac{F_1}{A_1(z)}\sin\theta_1(z) - (k_1 - m\omega_1^2)]dz \quad\quad (2.58)
$$

$$
\Gamma(z) = \frac{F_1}{A_1(z)\omega_1}\cos\theta_1(z) - b_1 \qu\quad (2.59)
$$

$$
|F_{pif}(z)| = A_2(z)\sqrt{m^2(\omega_2'^2 - \omega_2^2)^2 + b_2'^2\omega_2^2} \qu\quad (2.60)
$$

21

with

$$\omega'_2 = \sqrt{(k_2 - \frac{\partial F_c}{\partial z}|_z)/m}$$

$$b'_2 = b_2 - \Gamma(z). \tag{2.61}$$

The formalism outlined by Eqs. (2.58)-(2.60) makes it possible to reconstruct the distance dependent mechanical and photo-induced force from experimentally accessible parameters. Note that the Eq. (2.60) describes, in general, any driving force acting on the 2nd resonance of a cantilever with modulation frequency f_{02} as a function of A_1, ϕ_1 and A_2. One may apply this theoretical model to other systems to calculate the force acting on the 2nd resonance such as bimodal force microscopy, electric force microscopy, magnetic force microscopy and photo-induced force microscopy.

Chapter 3

Experiments and Discussion

3.1 Experimental methods

3.1.1 Light source

The reported experiments are carried out with a femtosecond light source. The pulsed light is derived from a ti:sapphire laser (MaiTai, Spectra-Physics), which delivers 200 fs pulses with a center wavelength of 809 nm. The pulse repetition rate is 80 MHz and the average power of the laser beam at the sample plane is 86 μW. The laser light is pre-compressed with a prism compressor to account for dispersion in the microscope optics. In addition, the laser light is amplitude modulated at a frequency that coincides with a higher-order mechanical resonance of the cantilever used in the experiment, as indicated below.

3.1.2 Atomic force microscope

A custom-modified atomic force microscope (Molecular Vista) is used for the photo-induce force experiments. A simplified scheme is given in Figure 3.5. The system consists of an inverted optical microscope outfitted with a $NA = 1.40$ oil immersion objective, a sample stage scanner, a AFM scan head and transmission and reflection optics for sample inspection. The microscope objective generates a diffraction-limited focal spot at the sample surface using x-polarized laser light. In the focal plane, significant portions of y-polarized and z-polarized light are present, which have distinct focal field distributions. The tip is positioned at the location of maximum z-polarized light [19] to enhance the sensitivity of the measurement to the z-directed gradient forces.

A 30 nm radius gold coated silicon tip is used in the experiments (FORTGG, AppNano). The cantilever system exhibits a mechanical resonance at $f_{01} = 58.58$ kHz with $k_1 = 1.6$ N/m and $Q_1 = 178$, operated with a free oscillation amplitude $A_{01} = 41$ nm. The photo-induced force measurements with this system are carried out at the third mechanical resonance of the cantilever, which is found at $f_{03} = 1033.190$ kHz. The corresponding spring constant and quality factor of this resonance are $k_3 = 492.51$ N/m and $Q_3 = 539$, respectively. The laser modulation frequency was set to 1033.190 kHz for photo-induced force measurements, coinciding with the third mechanical resonance of the cantilever.

The topographic and photo-induced force images are acquired simultaneously. This is achieved by demodulating the tip response at f_{01} to retrieve the topography image and at f_{02} (or f_{03}) to retrieve the photo-induced force image. The AFM controller of the Molecular Vista system includes a digital lock-in amplifier, used for demodulation of the signals, and a digital function generation with a field programmable gate array (FPGA), used for generating synchronized clock signals.

3.1.3 Sample materials

The test sample used in this study is a borosilicate coverslip with deposited nanoclusters of silicon naphtalocyanine (SiNc). The sample is prepared by spincasting a concentrated solution of SiNc in toluene onto the plasma-cleaned coverslip. After evaporation of the solvent, nanoscale aggregates of SiNc are formed, varying in size from several micrometers to less than 10 nm in diameter.

3.2 Linear optical response in photo-induced force microscopy

3.2.1 Force-distance simulations

We first study the general trends of the cantilever dynamics in the presence of both mechanical and photo-induced forces using Eqs (2.51)-(2.54). For this purpose, it is required to choose a functional form of the forces F_{int} and F_{pif} that are active at the tip-sample junction. We assume that F_{int} is described by a conservative Lennard-Jones-type force that contains a $1/z^6$ (repulsive) and a $1/z^2$ (attractive) force term,

$$F_{int} = f_0 \left(\frac{l^4}{3z^6} - \frac{1}{z^2} \right) \tag{3.1}$$

where f_0 is a constant and l is the characteristic distance at which the attractive force is minimized. For F_{pif} we obtain from Eqs. (2.28) and (2.9):

$$\langle \mathbf{F}_{PiF}(z) \rangle_z = -\frac{3\alpha_t' \alpha_p'}{2\pi\varepsilon_0 z^4} E_{0z}^2 + \frac{2\pi\alpha_t''}{\lambda} E_{0x}^2 \tag{3.2}$$
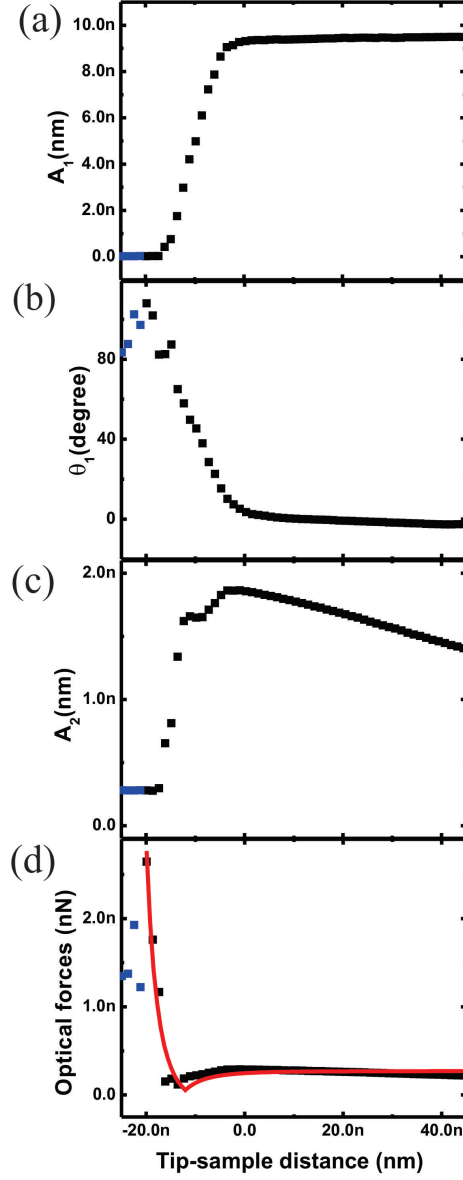
Figure 3.1: Simulation of the amplitude-distance curve (a) and the phase-distance curve of the fundamental resonance of a cantilever. The free oscillation amplitude of A_{01} is 20 nm. (c) Amplitude-distance curve of 2nd resonance of the cantilever for F_g with β (black) and 2β (red). (d) Pre-assumed Lennard-Jones type force (solid black) and the reconstructed force (purple dots). (e) Pre-assumed total magnitude of the optical force for β (solid black) and 2β (solid red), along with the corresponding reconstructed forces for β (purple dots) and 2β (green triangle). The experimental parameters of the simulation are given in [24].

Figure 3.1 shows the distance dependent amplitude (a) and the phase (b) of the first resonance, as well as the amplitude of 2nd resonance (c) as simulated with Eqs (2.51)-(2.54) and the chosen forces above. The z-dependent amplitude and phase of the first resonance show the expected profile for the chosen form of F_{int}. The amplitude of the second resonance, on the other hand, displays a very different profile, depicted by the black curve in Fig. 3.1(c). A peak near $z \approx 11$ nm is seen, the amplitude of which is dependent on the magnitude of the effective polarizability. Around $z \approx 15$ nm a sharp dip is observed, followed by a plateau at longer distances. Unlike the first resonance, the second resonance is sensitive to the presence of F_{pif}. The characteristic shape of the amplitude-distance curve reflects the presence of both the attractive gradient force and the repulsive scattering force. At shorter distances, the gradient force dominates, whereas for longer tip-sample separations the response is governed by the scattering force. The dip appears when the two photo-induced forces cancel, i.e. $F_g + F_{sc} = 0$.

The red curve in Fig. 3.1(c) is obtained by increasing the magnitude of F_g by a factor of two, i.e. β is twice as large as for the black curve, whereas F_{sc} remains the same. Two immediate changes are observed. First, the maximum amplitude A_2 is significantly larger for the 2β case, as can be expected for an increase in the magnitude of the gradient force. Second, the cancelation of the two optical forces now occurs at a longer distance, near ~ 18 nm rather than near ~ 15 nm in this simulation. An increase in the gradient force thus gives rise to an amplitude-distance curve that appears shifted to longer distances.

The formalism outlined in Eqs. (2.58)-(2.60) can be used to reconstruct the mechanical and optical forces between the tip and sample from the simulated amplitude-distance curves. The black solid line in Figure 3.1(d) represents the functional form of the assumed mechanical force, as given by Eq. (3.1). The purple dots indicate the reconstructed force from the simulated measurement. The close correspondence between the assumed and reconstructed data indicates that the assumptions made in (2.58)-(2.60) are justified. Similarly, the solid

black line in Figure 3.1(e) shows the chosen form of the optical force, described by Eq. (3.2), whereas the purple dots correspond to the reconstructed data. The simulated experiments presented in Figure 3.1 underline that the optical force can be extracted from measured amplitude-distances curves.

The red line in Figure 3.1(e) corresponds to the situation where β is twice as large as for the black solid line. Similarly to Fig. 3.1(c), the point where F_g and F_{sc} cancel lies at a longer distance. The shift of the cancelation point is a direct manifestation of the situation where F_g increases while F_{sc} remains constant. The set-point of the cantilever thus has a profound influence on the relative magnitude of the measured photo-induced forces. Consider the two curves in Figure 3.1(e), representing an object in the sample with β (black) and a second object with 2β (red). Depending on the set-point of the cantilever, the contrast between these two objects may vary drastically. For the values used in this simulation, if the set-point is at ~ 15 nm the force measured at the object represented by black curve is minimum while the net photo-induced force measured at the object with red curve is substantial. However, if the cantilever set-point is moved to 20 nm, the situation is reversed. The strongest force is now measured at the object with the weaker gradient force, as the net force at this distance is governed by F_{sc}. Hence, objects which give rise to a stronger F_g do not always produce the strongest signals in photo-induced force microscopy. The contrast observed is dependent on the cantilever set-point. Consequently, knowledge of the force-distance curve is essential for interpreting images generated with photo-induced force microscopy.

3.2.2 Photo-induced forces and molecular resonances

We next apply photo-induced force microscopy with fs pulse to visualize nanoscopic clusters of molecules. The sample used in this study is silicon naphtalocyanine (SiNc) molecules deposited on a glass coverslip. SiNc displays a strong absorption at 800 nm, which significantly
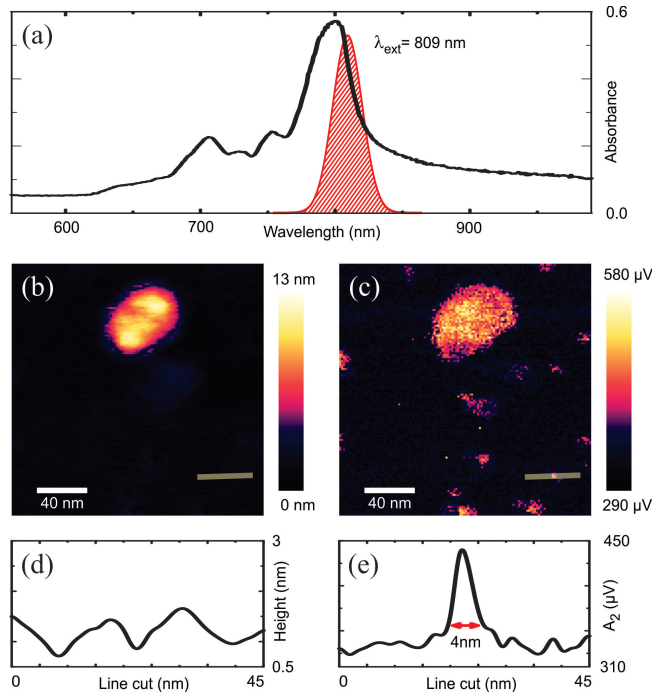
Figure 3.2: (a) Topography image of clusters of SiNc and (b) the corresponding photo-induced force image of SiNc. (c) One-dimensional cut at the line shown in the topography image (a). (d) One-dimensional cut at the line shown in the photo-induced force image (b).

overlaps with the spectrum of the laser pulses used. Figure 3.2(b) shows the topography image of a nanoscopic cluster of SiNc molecules on the glass surface. The corresponding photo-induced force image is shown in Figure 3.2(c). The photo-induced force image shows the same cluster as identified in the topography image. Whereas the topography image suggests height variations in the cluster, the photo-induced force image shows a nearly uniform signal in the cluster. This response is expected from the gradient force, which is a local force that is manifest close to the surface and relatively independent of volume effects. In addition to the larger cluster, smaller structures can be seen in Figure 3.2(c) which appear absent in the topography image. The one-dimensional line cuts shown in Figure 3.2(d) and (e) confirm that some smaller features are uniquely resolved in the optical force image. The width of these structures is < 10 nm, corresponding to the spatial resolution of the optical force microscope. Similar structures have been seen before in optical force microscopy, and have been suggested to originate from a single or a few molecules.[10]
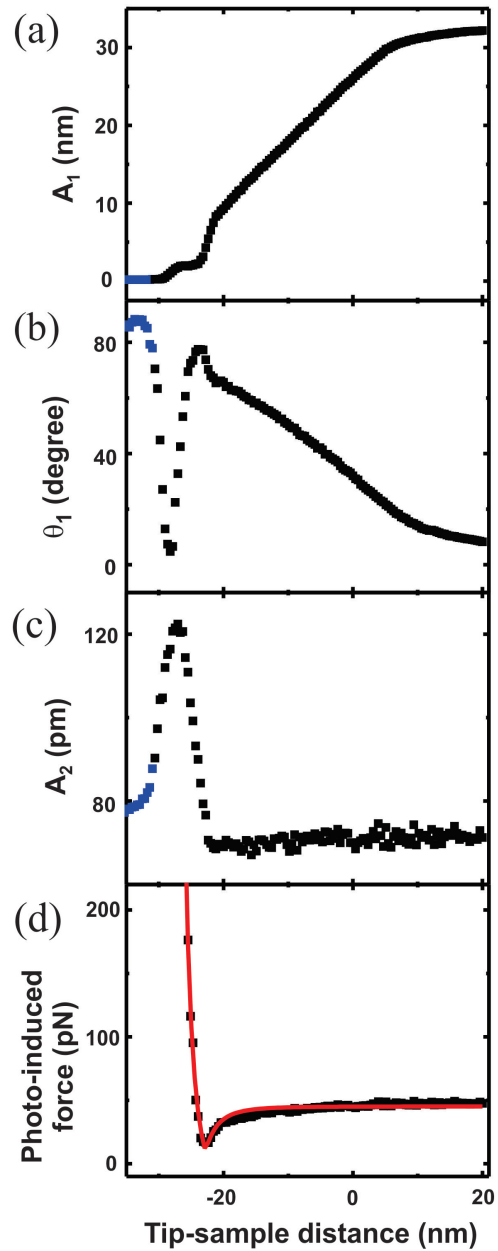
Figure 3.3: The amplitude (a) and the phase (b) of the fundamental resonance with respect to tip-sample distance on Si-naphthalocyanine (SiNc). The zero is the setpoint of tip is engaged. The sample is in negative side. The tip is retracted from the sample. (c) The amplitude of the 2nd resonance of the cantilever on SiNc. (d) The reconstructed optical forces on SiNc.

Figure 3.3(a) and (b) show the amplitude- and phase-distance curves, respectively, when the illuminated tip is positioned on the large cluster of molecules. These measurements help identify the onset of tip engagement and the regime in which hard-contact (blue data points) is reached. Photo-induced force measurements are performed by overlapping the laser modulation frequency with the third mechanical resonance of the cantilever at $f_{03} = 1033.190$ kHz. At this higher frequency, the effects of fluctuating thermal force contributions is expected to be reduced. The amplitude of the third mechanical resonance is shown in 3.3(c) and the extracted force is plotted in 3.3(d). Similar to the measurements on the gold nanowire, a clear dip can be seen in the force-distance curve, which is attributed to the cancellation of F_g and F_{sc}. Using Eq. (3.2), the force-distance curve can be fitted. From the fit, we find that $F_{sc} = 59.0$ pN and $\beta = 6.10 \times 10^{-43}$ N·m^4. Note that the β pre-factor in the SiNc measurements is smaller than in the measurements on gold, indicating that the gradient force between the tip and the SiNc is weaker than for the case of the gold nanowire.

In Figure 3.4 we compare the force-distance curve measured on another SiNc cluster with the force-distance curve recorded on the glass surface adjacent to the cluster. We observe that the cancelation point between F_g and F_{sc} appears for shorter tip-sample distances on the glass surface compared to when the tip is placed over the SiNc cluster. This is a consequence of the stronger F_g measured over the molecular cluster. To cancel out the stronger attractive force, the tip has to be moved farther from the sample, yielding an apparent shift of the dip in the force-distance curve.

The hard-contact region, where thermal expansion effects are most prominently measured, is clearly identified in the measurement. Fitting of the curves yields $\beta = 1.64 \times 10^{-42}$ N·m^4 for the SiNc cluster and $\beta = 1.75 \times 10^{-43}$ N·m^4 for the glass surface. The stronger gradient force for the molecular cluster is expected, as the molecular resonance dresses the material with a higher polarizability than the transparent glass material. The gradient force, therefore, is a sensitive probe of the optical properties of the sample under the tip. The scattering
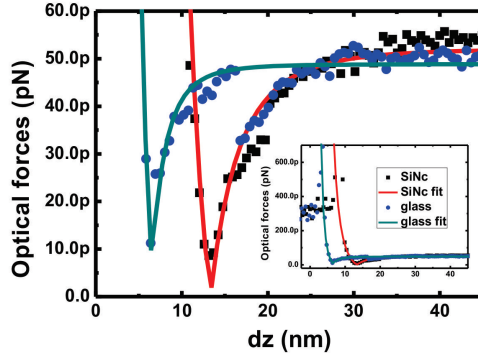
Figure 3.4: Comparison of the retrieved force-distance curves measured on SiNc and on glass.

force in both measurements, however, is comparatively similar: $F_{sc} = 52.1$ pN for the SiNc cluster and $F_{sc} = 45.3$ pN for the glass surface. Unlike the gradient force, the scattering force extends over a larger scale and is predominantly dictated by the optical response of the tip. The scattering force is relatively insensitive to the polarizability of the (molecular) sample, which is also evidenced by Eq. (2.9).

3.2.3 Photo-induced force microscopy with fs pulses

Unlike previous optical force experiments, which were carried out with cw illumination [10, 11], the force measurements reported here are conducted with 200 fs optical pulses derived from a ti:sapphire laser. Because of the much higher peak powers compared to cw irradiation, the use of fs pulses may raise concerns regarding optical nonlinearities at the tip that may negatively affect the stability and duration of the experiment. It is known that gold-coated tips exhibit plasmon resonances that can be driven at the excitation wavelength of 809 nm, which give rise to strong fields at the apex [22, 23]. Such high fields may induce nonlinear optical photodamage of the tip's nano-morphology, which in turn affects the effective polarizability of the tip and the optical force that results from it. In addition, unfavorable heat kinetics can give rise to time-varying thermal fluctuations on the time scale

of the experiment, which may overwhelm the cantilever dynamics driven by the pN optical forces.

However, our experiments suggest that optical force measurements can be confidently conducted with fs illumination. We find that keeping the illumination power well below 100 μW sustains stable conditions that enable force measurements over several hours. The use of a high-repetition rate laser is favorable in this regard, as a steady state in the tip-heating dynamics is achieved on the relevant time scale of the experiment. The ability to use fs pulsed excitation in optical force measurements opens exciting prospects for developing experiments where the measured force is induced by selected nonlinear optical manipulations of the sample.

3.3 Nonlinear optical response in photo-induced force microscopy

Femtosecond pump-probe measurement is one of the powerful tools for studying dynamic process of chemical materials at ultrafast time scale. This enables to follow in real time vibrational motions coupled to electronic transitions. However, the pump-probe type measurement has been limited at smaller scale because of the signal to noise ratio which is depended on the change of the number of photons. Measuring the photon change in single molecule level is very difficult with nominal optical detector. Hence, it is necessary to develop the background-free measurement. In this regard, recent developments in combining photo-induced molecular excitations with mechanical force detection are of particular interest, as these approaches seek to add chemical selectivity to force microscopy [7, 9, 10, 11].

A successful example in this category of techniques is photo-induced force microscopy, which probes the photon-induced changes in the dipolar interactions between a sharp polarizable tip
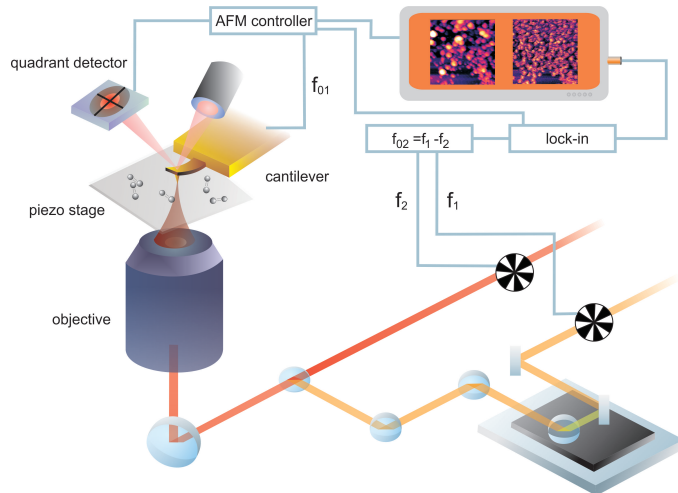
Figure 3.5: Sketch of the optical force microscope

and the sample [10, 11]. The contrast in photo-induced force microscopy is directly sensitive to the electromagnetic forces at play in the tip-sample junction, and can, in principle, be conducted in non-contact mode AFM. The advantage of this approach is that any optical transitions – linear and nonlinear – can be probed directly as dissipation of excitation energy in the material. Yet, this promising technique hasn't proven to perform with the pump-probe technique to explore time- and spectral-resolved dynamics of chemical information. In this contribution, we provide an ultrafast time-resolved pump-probe measurement in terms of classical fields and forces.

The concept of this scheme can be understood by referring to Figure 3.5. Two 200 fs pulse beams derived from a ti:sapphire laser – a pump beam at frequency ω_1 and a probe beam at frequency ω_2 – are arranged via optical parametric oscillator (OPO) into the objective. They are focused to a diffraction limited spot on the tip-molecule junction to efficiently stimulate molecular excitations at frequency (ω_1-ω_2). When we approach a cantilevered, gold coated, scanning probe microscope tip to the oscillating molecule within nm range, the illuminated beams on the tip-molecule junction result in induced dipoles on the molecule and on the tip. These induced dipoles mutually interact to each others, and the field-gradient between them results in the dipole-dipole force [28, 10, 11**?**]. In general a time-averaged conservative
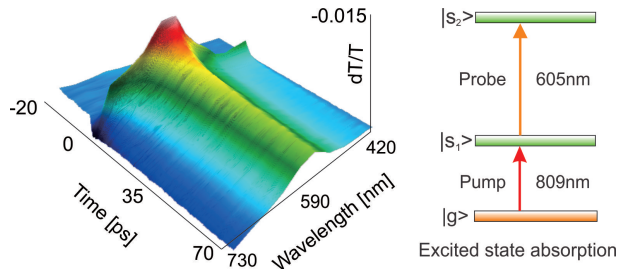
34

Figure 3.6: Time- and spectral-resolved curves of SiNc via photodiode detector.

photo-induced dipole force can be described as

$$\langle \mathbf{F} \rangle = -\nabla_{\mathbf{r}} \Re \int d\omega \vec{\mu}(\omega) \cdot \mathbf{E}(\mathbf{r}, \omega) \tag{3.3}$$

where $\vec{\mu}$ is an induced dipole of molecule, $\mathbf{E}$ is the total electric field between dipoles, $\mathbf{r}$ is a distance between two dipoles.

The power of each illuminated beams are modulated with frequency f_1 (pump) and f_2 (probe) respectively. The force interaction between the dipole on the excited oscillating molecules and the one on the tip is modulated at 2nd mechanical resonance f_{02} such that $f_{02} = f_1 - f_2$. The topographic image (with the fundamental resonance f_{01}) and the photo-induced dipole force image (with the 2nd resonance f_{02}) are acquired simultaneously. Note that any nonlinear pump-probe optical transitions – excited state absorption and Raman – of molecules can be probed directly when the optical difference frequency $(\omega_1\text{-}\omega_2)$ is set to demand chemistry. This photo-induced force signal is enhanced by the plasmonic-field at the end of tip and amplified with the 2nd mechanical resonance so that the signal to noise ratio is drastically increased. According to our previous work on force detection of molecules driven at their electronic resonance [28, 10, 11], for the gold coated sharp tip, we estimate the pump-probe force to be around 10^{-11}N whereas the minimum detectable force is around 10^{-13}N.

A custom-modified non-contact/tapping-mode atomic force microscopes (VistaScope from
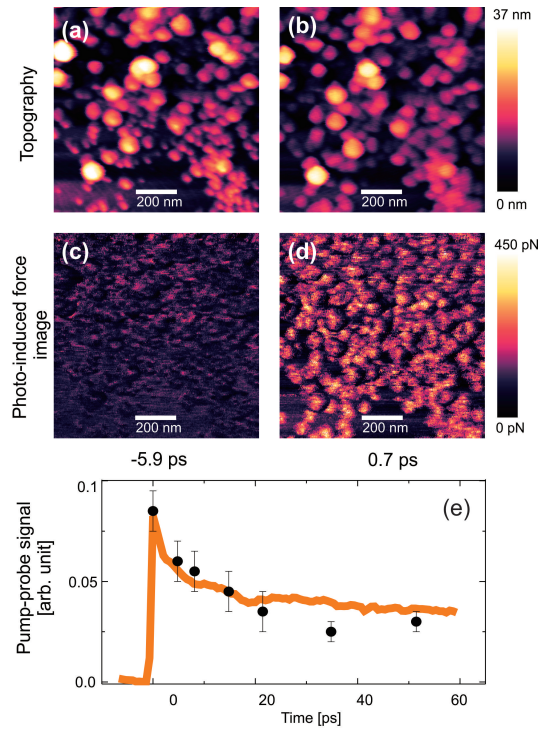
Figure 3.7: The topography image (a) (or (b)) and optical force image (c) (or (d)) are simultaneously recorded at negative time difference -5.9 ps (or positive time difference 0.7 ps). (e) direct comparison between the photodiode detector (orange solid line) and optical force (black circle dots).

Molecular Vista Instrument and FlexAFM from Nanosurf) and a ti:sapphire laser (MaiTai, Spectra-Physics) whose pulse repetition rate is 80 MHz are used for the photo-induced force measurements. The average power of two laser beams through oil-immersion objective (NA=1.4) is nominally adjusted 50 μ each at the sample plane. The laser light is pre-compressed with a prism compressor to account for dispersion in the microscope optics. We chose a cantilever with $f_{01} = 178$ kHz, quality factor $Q_1 = 490$ and stiffness constant $k_1 = 58$ N/m of a fundamental resonance, and $f_{02} = 1098$ kHz, quality factor $Q_2 = 588$ and stiffness constant $k_2 = 2267$ N/m of a 2nd resonance, operated with a free oscillation amplitude of fundamental resonance $A_{01} = 47$ nm. We chose $f_1 = 1000$ kHz for 809nm (pump) and $f_2 = 2098$ kHz for 605nm (probe) so that $f_2 - f_1 = 1098$ kHz and the sideband coupled modulation coincided with the second mechanical resonance f_{02} of the cantilever.

The deposited nanoclusters of silicon naphtalocyanine (SiNc) on a borosilicate coverslip is used for the excited state transition-induced force measurement. The sample is prepared by spincasting a concentrated solution of SiNc in toluene onto the plasma-cleaned coverslip. After evaporation of the solvent, nanoscale aggregates of SiNc are formed, varying in size from several micrometers to less than 10 nm in diameter.

The time- and spectral-resolved excited state absorption curves of bulk SiNc via a photodiode detector is shown in Figure 3.6, which is obtained with fully optical microscope. The pump beam excited the ground state electrons to the 1st excited state, then the probe beam excited the electrons to the 2nd excited state. SiNc displays a strong excited state absorption with 809nm pump and 605nm probe. The negative time means that there is the probe beam before the pump beam so that the time delay is negative. Note that the excited state absorption process of SiNc is disappeared at negative time.

The nanoscale time-resolved photo-induced force images of SiNc molecules are displayed in Figure 3.7. The topography images (a) or (b) and photo-induced force images (c) or (d) are simultaneously recorded at negative time difference -5.9 ps or positive time difference 0.7 ps

respectively. Note that the contrast of the photo-induced force image is clearly shown at positive time rather than the one at negative time. The photo-induced force image shows the same cluster as identified in the topography image. Whereas the topography image suggests height variations in the cluster, the photo-induced force image shows a nearly uniform signal in the cluster. This response is expected from the gradient force, which is a local force that is manifest close to the surface and relatively independent of volume effects [28, 10]. In addition to the larger cluster, smaller structures can be seen in Figure 3.7(d) which the width of these structures is ~ 10 nm, which corresponds to the spatial resolution of the photo-induced force microscope.

Figure 3.7(e) directly compares the all-optical measurement to the photo-induced force measurement at 809nm pump and 605nm probe beams. The orange solid line is the excited state absorption curve of bulk SiNc via a photodiode detector. The black circle dots are the localized nonlinear photo-induced force signal due to the excited state transition dipole on another SiNc cluster sample via the photo-induced force microscopy. Each vertical scales are adjusted for comparison. They are excellently correspond to each other.

Chapter 4

Conclusion and Future works

In this work, we have studied the mechanisms that contribute to the signals measured in optical force microscopy. This new form of microscopy operates in a regime away from the hard-contact mode, as is required in IR AFM techniques. Consequently, thermal expansion of the sample after optical excitation is not the primary contrast mechanism in optical force microscopy. Instead, the technique is directly sensitive to the electromagnetically induced forces in the tip-sample junction, as described by the gradient force F_g and the scattering force F_{sc}. Optical force microscopy enables the measurement of F_g and F_{sc}, and generates images with contrast based on the spatial variation of these two optical forces.

We have provided a theoretical description of cantilever dynamics in the presence of F_{opt}, the sum of F_g and F_{sc}. The optical force is conveniently detected at modulation frequencies that coincide with higher-order resonances of the cantilever system. The amplitude of the cantilever at the frequency of the higher-order mechanical resonance reflects the competition between the attractive gradient force and the repulsive scattering force. The simulated amplitude-distance curve reveals a minimum at the tip-sample distance where F_g and F_{sc} cancel. The z-distance at which the minimum occurs may change as a function of lateral

position in the sample, as the relative contributions of F_g and F_{sc} may vary from point to point. Therefore, the positive (attractive) contrast in optical force microscopy is dictated by the spatial variation of F_g relative to F_{sc}.

Our formulation allows the reconstruction of the optical forces from amplitude-distance measurements. Experiments on bare glass, gold nanowires and molecular clusters confirm that F_g and F_{sc} manifest themselves on different spatial scales. Fits to the reconstructed force-distance curves indicate that F_g is local and, because of the z^4-dependence, significant only for tip-sample distances within a few nm. In addition, F_g is sensitive to the polarizability of the sample object. For instance, the polarizability of the glass surface at the 809 nm excitation wavelength is significantly lower than the polarizability of the optically-resonant SiNc nanocluster, resulting in a much stronger measured F_g for the latter. The scattering force, on the other hand, shows no distance dependence on the nanoscale. This observation complies with the theoretical description of F_{sc} in Eq. (2.9), which states that it is manifest over a length scale defined by the axial extent of the optical excitation field ($\sim \mu$m).

Whereas F_g varies dramatically with the polarizability of the sample, the measurements reveal that F_{sc} is in the 40 – 50 pN range for all measurements presented here. This is to be expected from Eq. (2.9), which indicates that the magnitude of the scattering force is defined by the interaction of the excitation light with the tip. Naturally, the magnitude of F_{sc} is a direct function of the tip material and morphology. The different distance-dependence and polarizability-dependence of F_g and F_{sc} gives rise to a force-distance curve that can vary dramatically from point to point. The contrast in the image is also dependent on the set-point of the cantilever. Changing the set-point may change the contrast of a given object on the glass surface from positive to negative relative to the signal from the glass. This notion emphasizes that understanding the mechanisms at play in optical force microscopy is essential for interpreting the images produced with this technique.

We also have shown that the nonlinear optical response such as the excited state absorption

and the stimulated Raman effect can be detected through an entirely different channel–namely, photo-induced force microscopy, by measuring the force between a nonlinear excited molecular feature and a gold coated probe tip in a scanning probe microscope. This new form of microscopy operates in a regime away from the hard-contact mode, as is required in photo-thermal infrared AFM techniques [7, 9]. While apertureless near-field microscopes based on light scattering from tips have had great success in imaging nanoscopic objects from the visible to the infrared, including the Raman effect through fluorescence, the signals are very weak since they are based on far-field optical detection of a near-field interaction [25]. We believe that our approach – measuring optical response with non-optical method – can be readily extended to a single molecule level and may track conformational changes within a molecule. The ability to apply the AFM for nanometer scale optical spectroscopic analysis opens new opportunities in materials science and biology by probing nonlinear optical excitations in individual molecules.

Bibliography

[1] *"Colloquium*: Gripped by light: Optical binding", Rev. Mod. Phys., **82**, 1767 (2010).

[2] Ashkin, A. Acceleration and trapping of particles by radiation pressure. Phys. Rev. Lett. **24**, 156159(1970).

[3] L. Gross, F. Mohn, N. Moll, B. Schuler, A. Criado, E. Guitian, D. Pena, A. Gourdon, and G. Meyer, "Bond-order discrimination by atomic force microscopy," Science, **337**, 1326-1329 (2012).

[4] J. Zhang, P. Chen, B. Yuan, W. Ji, Z. Cheng, and X. Qiu, "Real-space identification of intermolecular bonding with atomic force microscopy," Science, **342**, 611-614 (2013).

[5] A. Dazzi, R. Prazeres, F. Glotin, and J. M. Ortega, "Subwavelength infrared spectromicroscopy using an AFM as a local absorption sensor," Infrared Phys. Technol. **49**, 113-121 (2006).

[6] A. Dazzi, F. Glotin, and R. Carminati, "Theory of infrared nano spectroscopy by photo thermal induced resonance," J. Appl. Phys. **107** 124519 (2010).

[7] A. Dazzi, C. B. Prater, Q. Hu, D. B. Chase, J. F. Rabolt, and C. Marcott, "AFM-IR: Combining atomic force microscopy and infrared spectroscopy for nanoscale chemical characterization," Appl. Spectrosc. **66**, 1365-1384 (2012).

[8] A. M. Katzenmeyer, V. Aksyuk, and A. Centrone, "Nanoscale infrared spectroscopy: improving the spectral range of the photo thermal induced resonance technique," Anal. Chem. **85**, 1972-1979 (2013).

[9] F. Lu, M. Jin, and M. A. Belkin, "Tip-enhanced infrared nanospectroscopy via molecular expansion force detection," Nature Phot. **8**, 307-312 (2014).

[10] I. Rajapaksa, K. Uenal, and H. K. Wickramasinghe, "Image force microscopy of molecular resonance: A microscope principle," Appl. Phys. Lett. **97**, 073121 (2010).

[11] I. Rajapaksa, K. Uenal, and H. K. Wickramasinghe, "Raman spectroscopy and microscopy based on mechanical force detection," Appl. Phys. Lett. **99**, 161103 (2011).

[12] P. Suarabh, and S. Mukamel, "Atomic force detection of single-molecule nonlinear optical vibrational spectroscopy," J. Chem. Phys. **140**, 161107 (2014).

[13] L. Novotny and B. Hecht, *Principles of Nano-Optics*, Cambridge (2006).

[14] R. Garcia and E. T. Herruzo, "The emergence of multifrequency force microscopy," Nature Nanotech. **7**, 217–226 (2012).

[15] J. N. Israelachvili, *Intermolecular and Surface Forces* (Academic Press, New York, 1994).

[16] R. Garcia and R. Perez, "Dynamic atomic force microscopy methods," Surf. Sci. Rep. **47**, 197–301 (2002).

[17] J. E. Sader and S. P. Jarvis, "Accurate formulas for interaction force and energy in frequency modulation force spectroscopy," Appl. Phys. Lett. **84**, 1801 (2004).

[18] J. E. Sader, T. Uchihashi, M. J. Higgins, A. Farrell, Y. Nakayama, and S. P. Jarvis, "Quantitative force measurements using frequency modulation atomic force microscopy - theoretical foundations," Nanotechnology **16**, S94 (2005).

[19] A. Bouhelier, M. Beversluis, A. Hartschuh, and L. Novotny, "Near-field second-harmonic generation induced by local field enhancement," Phys. Rev. Lett. **90**, 013903 (2003).

[20] M. Lee and W. Jhe, "General theory of amplitude-modulation atomic force microscopy," Phys. Rev. Lett. **97**, 036104 (2006).

[21] E. J. Menke, M.A. Thompson, C. Xiang, L C. Yang, and R. M. Penner, "Lithographically patterned nanowire electrodeposition," Nature Mat. **5**, 914-919 (2006).

[22] M. I. Stockman, "Nanofocusing of optical energy in tapered plasmonic waveguides," Phys. Rev. Lett. **93**, 137404 (2004).

[23] S. Berweger, J. M. Atkin, R. L. Olmon, and M. B. Raschke, "Light on the tip of a needle: plasmonic nanofocusing for spectroscopy on the nanoscale," J. Phys. Chem. Lett. **3** 945–952 (2012).

[24] $f_0 = 3 \times 10^{-27}$ N $\cdot$ m^2, $l = 2.34 \times 10^{-8}$m, $F_1 = 16 \times 10^{-11}$ N, $\beta = 5 \times 10^{-43}$ N$\cdot$m^4, $k_1 = 1.6$ N/m, $k_2 = 62.9$ N/m, $\omega_{01} = 60$ kHz, $\omega_{02} = 376.2$ kHz, $Q_1 = 200$, $Q_2 = 1254$, $F_{sc} = 1 \times 10^{-11}$ N.

[25] H. J. Mamin and D. Rugar, "Sub-attonewton force detection at millikelvin temperatures," Appl. Phys. Lett. **79**, 3358 (2001).

[26] R. W. Stark and W. M. Heckl, "Fourier transformed atomic force microscopy: tapping mode atomic force microscopy beyond the Hookian approximation," Surf. Sci. **457**, 219 (2000).

[27] J. E. Sader, I. Larson, P. Mulvaney, and L. R. White, Rev. Sci. Instrum. **66**, 3789 (1995).

[28] Junghoon Jahng, Jordan Brocious, Dmitry A. Fishman, Fei Huang, Xiaowei Li, Venkata Ananth Tamma, H. Kumar Wickramasinghe, and Eric O. Potma, "Gradient and scattering forces in photoinduced force microscopy," Phys. Rev. B **90**, 155417 (2014).

[29] Tetsuhiro Kudo and Hajime Ishihara, "Resonance optical manipulation of nano-objects based on nonlinear optical response", Phys. Chem. Chem. Phys., **15**, 14595–14610 (2013).